ARTICLES
https://doi.org/10.1038/s41565-022-01079-3
nature nanotechnology

Check for updates

Polarization-sensitive optoionic membranes from chiral plasmonic nanoparticles

Jiarong Cai[1,2,15], Wei Zhang[3,4,15], Liguang Xu[1,2,5,15], Changlong Hao[1,2], Wei Ma[1,2], Maozhong Sun[1,2], Xiaoling Wu[1,2], Xian Qin[6], Felippe Mariano Colombari[7], André Farias de Moura[8], Jiahui Xu[6], Mariana Cristina Silva[8], Evaldo Batista Carneiro-Neto[8], Weverson Rodrigues Gomes[8], Renaud A. L. Vallée[9], Ernesto Chaves Pereira[8], Xiaogang Liu[6], Chuanlai Xu[1,2,5] ✉, Rafal Klajn[10] ✉, Nicholas A. Kotov[11,12,13] ✉ and Hua Kuang[1,2,5,14] ✉

Optoelectronic effects differentiating absorption of right and left circularly polarized photons in thin films of chiral materials are typically prohibitively small for their direct photocurrent observation. Chiral metasurfaces increase the electronic sensitivity to circular polarization, but their out-of-plane architecture entails manufacturing and performance trade-offs. Here, we show that nanoporous thin films of chiral nanoparticles enable high sensitivity to circular polarization due to light-induced polarization-dependent ion accumulation at nanoparticle interfaces. Self-assembled multilayers of gold nanoparticles modified with L-phenylalanine generate a photocurrent under right-handed circularly polarized light as high as 2.41 times higher than under left-handed circularly polarized light. The strong plasmonic coupling between the multiple nanoparticles producing planar chiroplasmonic modes facilitates the ejection of electrons, whose entrapment at the membrane–electrolyte interface is promoted by a thick layer of enantiopure phenylalanine. Demonstrated detection of light ellipticity with equal sensitivity at all incident angles mimics phenomenological aspects of polarization vision in marine animals. The simplicity of self-assembly and sensitivity of polarization detection found in optoionic membranes opens the door to a family of miniaturized fluidic devices for chiral photonics.

Interactions between circularly polarized light (CPL) and matter hold promise for many emerging technologies[1–3]. However, for optoelectronic thin films of chiral organic materials or inorganic nanoparticles (NPs), the difference in light absorption between left- (L) and right- (R) handed photons typically does not exceed a fraction of a percent, which is prohibitively small for polarization-sensitive photocurrent devices[4]. Metamaterials and metasurfaces with nanoscale geometries matching helical field distribution of CPL increase the sensitivity of light–matter interactions to circular polarization[5–9]. However, the out-of-plane engineering of these metastructures results in both performance and manufacturing trade-offs, hindering the conversion of optical absorption into electron transport and imparting strong angular dependence[4].

Similar to the coupling of CPL with electron clouds in molecules, coupling of spin-angular momentum of photons with the transport of ion clouds in electroactive nanoscale pores can lead to optoelectronic effects[10–15]. Of particular interest are bioinspired light-sensitive nanoscale channels[16–20], with some of them replicating membranes of retinal cells[21–23], but photocurrents or photovoltages generated across them are not known to be CPL dependent[24–26]. Here, we show that the optoionic phenomena in thin nanoscale membranes from chiral gold NPs lead to unexpectedly high sensitivity to circular polarization of incident photons. When NPs in the self-assembled membranes (nanofilms) are decorated by L-phenylalanine (Phe), the photoinduced current (photocurrent) across the layer under right-handed circularly polarized (RCP) illumination is 1.47, 1.87, 2.20 and 2.41 times that under left-handed circularly polarized (LCP) illumination for monolayer (1L), three-layer (3L), five-layer (5L) and ten-layer (10L) nanofilms, respectively (Fig. 1a). Experimental and computational studies show that polarization-dependent transduction of CPL incident onto the multilayer NP membranes into photocurrent across thin films of chiral NPs originates from the light-driven ejection of electrons facilitated by the strong plasmonic modes coupled within the plane of the nanofilms. The thick surface layer of enantiopure Phe ligands on the NP surface extends the lifetime of the ejected electrons, while the photoinduced charge accumulated at the interfaces causes reorganization of the ionic atmosphere in the nanoscale channels. These optoionic effects can be utilized in a wide range of microfabricated fluidic devices.

[1]State Key Laboratory of Food Science and Technology, Jiangnan University, Wuxi, China. [2]International Joint Research Laboratory for Biointerface and Biodetection, School of Food Science and Technology, Jiangnan University, Wuxi, China. [3]Institute of Applied Physics and Computational Mathematics, Beijing, China. [4]Beijing Computational Science Research Centre, Beijing, China. [5]The Key Laboratory of Synthetic and Biological Colloids, Ministry of Education, School of Chemical and Material Engineering, Jiangnan University, Wuxi, China. [6]Department of Chemistry, National University of Singapore, Singapore, Singapore. [7]Brazilian Biorenewables National Laboratory, Brazilian Center for Research in Energy and Materials, Campinas, Brazil. [8]Department of Chemistry, Federal University of São Carlos, São Carlos, Brazil. [9]CNRS, University of Bordeaux, Pessac, France. [10]Department of Molecular Chemistry and Materials Science, Weizmann Institute of Science, Rehovot, Israel. [11]Department of Chemical Engineering, University of Michigan, Ann Arbor, MI, USA. [12]Biointerfaces Institute, University of Michigan, Ann Arbor, MI, USA. [13]Michigan Institute for Translational Nanotechnology, Ypsilanti, MI, USA. [14]Science Center for Future Foods, Jiangnan University, Wuxi, China. [15]These authors contributed equally: Jiarong Cai, Wei Zhang, Liguang Xu. ✉e-mail: xcl@jiangnan.edu.cn; rafal.klajn@weizmann.ac.il; kotov@umich.edu; kuangh@jiangnan.edu.cn

Results and discussion

Chiral nanomembranes. L-Phe- and D-Phe-modified spherical Au NPs, 35 nm in diameter, were assembled at a liquid–liquid interface to form NP monolayers[27–29], which were subsequently transferred onto anodized aluminium oxide (AAO) or glass slides for electrochemical or optical measurements using the Langmuir–Blodgett technique. The surfaces of the NP monolayers were uniform over an area of at least several square centimetres and displayed a distinct metallic lustre. Scanning electron microscopy (SEM) and atomic force microscopy (AFM) images of the cross-sections and surfaces of all nanofilms showed densely packed NPs, with nanoscale channels formed between them (Fig. 1b and Supplementary Fig. 1).

The circular dichroism (CD) spectra of L-Phe- and D-Phe-modified NP films displayed amplitudes approaching 350 mdeg at a wavelength of 762 nm (Fig. 1f), whereas nanofilms of Au NPs carrying achiral citrate (Cit) or DL-Phe ligands (that is, a racemic 1:1 mixture of L- and D-Phe) showed near-zero CD spectra (Supplementary Fig. 2). The strong chiroptical activity of these nanofilms is attributed to the coupling of the molecular-scale chirality of Phe and the surface plasmon modes of metallic NPs[30–32] in the highly polarizable gold nanofilms[33,34]. Note also that modes localized in the gaps in the planar arrays of plasmonic particles are further enhanced by the short-range order observed for the nanofilms[35–38]. Taking the nanofilm model based on experimental AFM imaging, the chiroplasmonic lattice modes can be visualized by electrodynamic and finite-difference time-domain (FDTD) simulations (Fig. 1c,d). The FDTD-calculated CD spectrum matches nearly perfectly with the experimental data (Fig. 1g), verifying the origin of strong CD bands and the optoionic effects. The simulations also show that these modes have distinct wave-guided behaviour[39] propagating along their surface (Fig. 1e). Importantly, such modes concentrate the field and optical energy exactly where the density of the particle–electrolyte interface is the highest, facilitating the coupling of photonic and ionic processes in the electric double layers around the nanoparticles, while reducing the far-field optical scattering along the direction normal to the nanofilm surface.

Photocurrent generation. The photocurrent, I, was measured for monolayers and multilayers of NPs illuminated by 808 nm light (10 mW cm^{-2}) over periods of 60 s. The nanofilms were deposited on AAO supports placed between two compartments filled with an aqueous electrolyte (Fig. 1a). Photocurrent $I(t)$ curves and maximal amplitudes (denoted as $I_{||}$, I_L and I_R, respectively) were recorded for linearly polarized (LP), LCP and RCP light. The nanofilms from L-Phe -NPs displayed a photocurrent of $I_R = 10.04 \pm 1.25$ nA under RCP irradiation, that is, considerably larger than that under LCP illumination; $I_L = 6.82 \pm 1.14$ nA. Nanofilms from D-Phe-NPs exhibited $I_L = 10.35 \pm 1.08$ nA and $I_R = 6.87 \pm 0.95$ nA under LCP and RCP, respectively, displaying a distinct mirror-symmetrical relationship between I and the chirality of Phe (Fig. 1h,i). Concurrently[17], the photovoltage–time curves featured a similar change trend and mirror symmetry relationship with the photocurrent (Fig. 1j,k). In control experiments, an AAO membrane without the nanofilm or under other conditions (for example, nanofilms of Cit-NPs or DL-Phe-NPs) displayed little or no change in current across the membrane (Supplementary Fig. 3). No evidence of physical erosion or chemical deterioration of the nanofilms in the electrolyte solution with and without light was observed (Supplementary Fig. 4).

By analogy to CD spectroscopy, $\Delta I_{L-R} = I_L - I_R$ can be used to characterize the polarization dependence of the photocurrent on nanofilm structure and other factors. Illumination at 808 nm was used in most experiments because it produced the highest I and ΔI_{L-R} values (Fig. 2a and Supplementary Fig. 5). Nanofilms of 35 nm Au NPs displayed higher ΔI_{L-R} values than NPs of other sizes (Fig. 2b and Supplementary Fig. 6). We also tested the illumination intensities from 1 to 20 mW cm^{-2} (Fig. 2c and Supplementary Fig. 7) and illumination times from 0 to 60 s (Fig. 2d and Supplementary Fig. 8); ΔI_{L-R} reached a maximum of 3.22 ± 0.15 nA after continuous illumination for 60 s (10 mW cm^{-2}). Even for a single NP monolayer, the photocurrent under RCP was 1.47-fold higher in magnitude than under LCP, which markedly exceeds the subpercentile differences in RCP versus LCP adsorption in thin films of chiral materials. Importantly, it also exceeds the photocurrents generated in metamaterials[40,41].

Uniqueness of nanofilms from enantiopure Phe-NPs. To shed light on the polarization dependence of the photocurrent, I and ΔI_{L-R} values of nanofilms modified at different concentrations of L-Phe were analysed. As the L-Phe concentration increased, the amplitude of the chiroplasmonic peak increased from 0 to 350 mdeg at 762 nm, reaching a plateau at 30 mM L-Phe (Fig. 3a). ΔI_{L-R} increased in the same progression and retained a perfect mirror-image symmetry (Fig. 3b and Supplementary Fig. 9). One might expect to see similar amplitudes of ΔI_{L-R} and maxima of CD spectra and concentration dependence for other chiral amino acids, but that was not the case. Surprisingly, however, all 15 seemingly similar surface ligands displayed CD peaks smaller by more than an order magnitude (<25 mdeg) and near-zero ΔI_{L-R} (Fig. 3c and Supplementary Fig. 10).

Structural reasons for the uniqueness of Phe-NP nanofilms can be understood by analysing high-resolution transmission electron microscopy (HRTEM) images of several types of NPs. An unexpectedly thick organic layer was observed on the NPs modified with L-Phe and D-Phe, whereas the layers of surface ligands on all the other NPs were nearly indistinguishable with HRTEM (Fig. 3d). As the L- or D-Phe concentration for Cit-NP modification before nanofilm preparation increased from 10 to 30 mM, the thickness of the organic layer on the NP surface increased from ~0.8 to 2.3 nm and remained unchanged above 30 mM. Our data show that the thickness of the surface layer correlated directly with both the amplitude of the CD peak and ΔI_{L-R} (Fig. 3e and Supplementary Fig. 11). Formation of the organic layer on NP surfaces is attributed to facile D- or L-Phe self-limited self-assembly into non-covalently bonded multilayers (Supplementary Table 1 and Supplementary Figs. 12 and 13)[42–45]. The weak CD and near-zero ΔI_{L-R} values of

Fig. 1 | Polarization-sensitive optoionic effects in nanofilms from chiral plasmonic NPs. a, Schematic illustration of the electrochemical cell used in the study. The photoinduced current generated across the membranes was greater for RCP illumination than for LCP illumination in nanofilms made from L-Phe-NPs. The opposite was true for nanofilms made from D-Phe-NPs. **b**, Structural characterization of nanofilms. Photograph of the photosensitive membranes (diameter 12 mm) carrying a nanofilm from L-Phe-NPs (left). SEM image of the cross-section of the AAO membrane with the nanofilm on top (middle). SEM image of the monolayer L-Phe-NP film (right). **c**, 3D tomographic image of a monolayer of L-Phe-NP film. **d**, Schematic illustration of the model system used in the electrodynamics simulations in **e**. **e**, Vectors depicting the electric field of the LCP photons at 690 nm that were scattered by the model L-Phe-NP film in **d**. The NPs are depicted as black dashed lines, and vectors pointing in the z direction stand for the photons that have been scattered at angles close to 90° and are moving inside the membrane, which acts as a wave guide. **f**,**g**, Experimental (**f**) and calculated (**g**) CD spectra for nanofilms from L-Phe-NP and D-Phe-NP. **h**,**i**, Temporal profile of the photocurrent across the photosensitive membrane with nanofilms from L-Phe-NPs (**h**) and D-Phe-NPs (**i**). **j**,**k**, Temporal profile of the photovoltage across the photosensitive membrane with nanofilms from L-Phe-NPs (**j**) and D-Phe-NPs (**k**) induced with CPL illumination (10 mW cm^{-2}) at 808 nm.

the other 15 chiral ligands also confirm that the organic layer on the Phe-modified NPs dictates their chirality and the photocurrent in the nanofilm.

Mechanism of CPL-dependent photocurrent generation. We initially hypothesized that the unusually large effect of circular polarization on the photocurrent in nanofilms was attributable to local

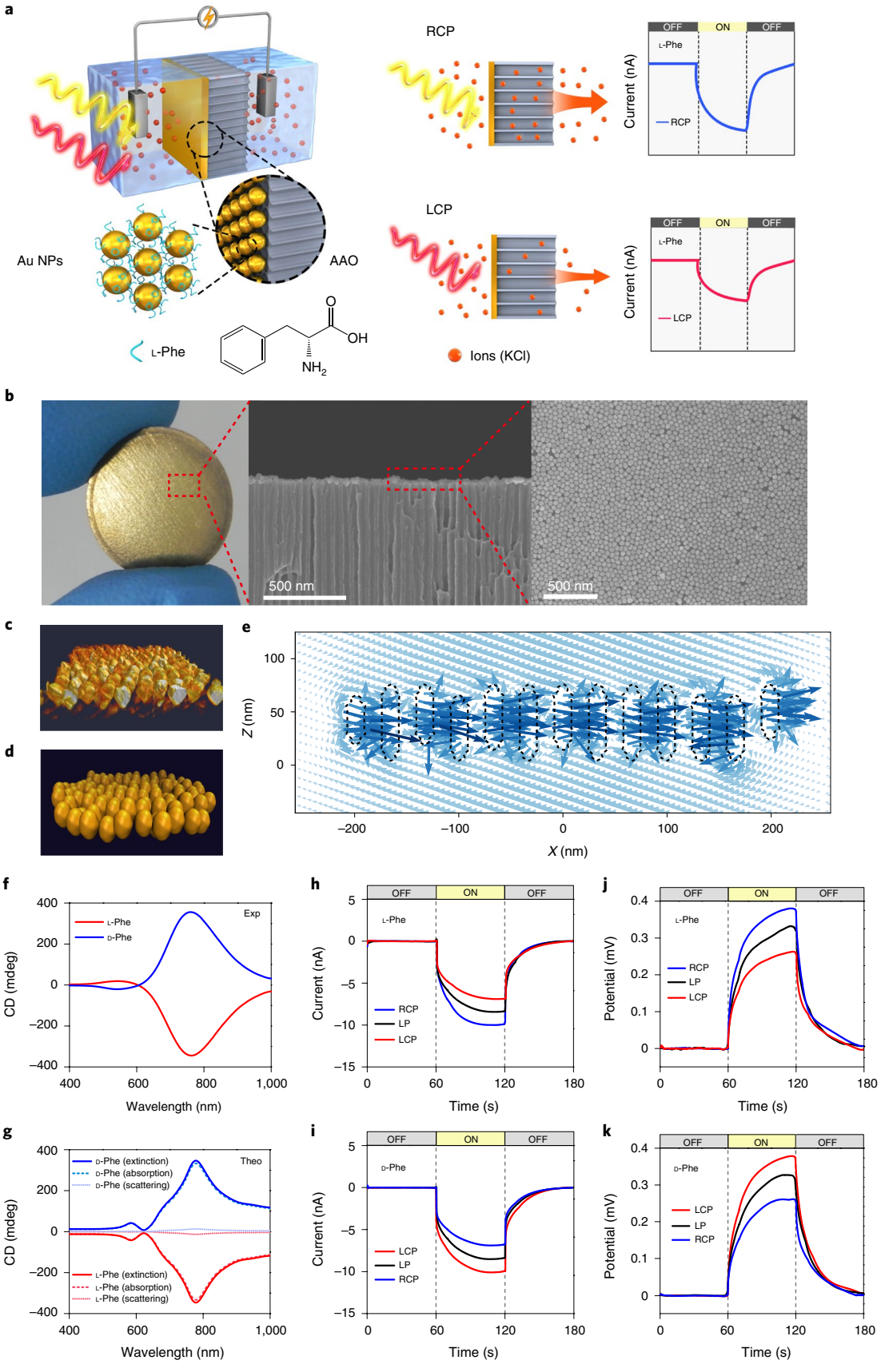

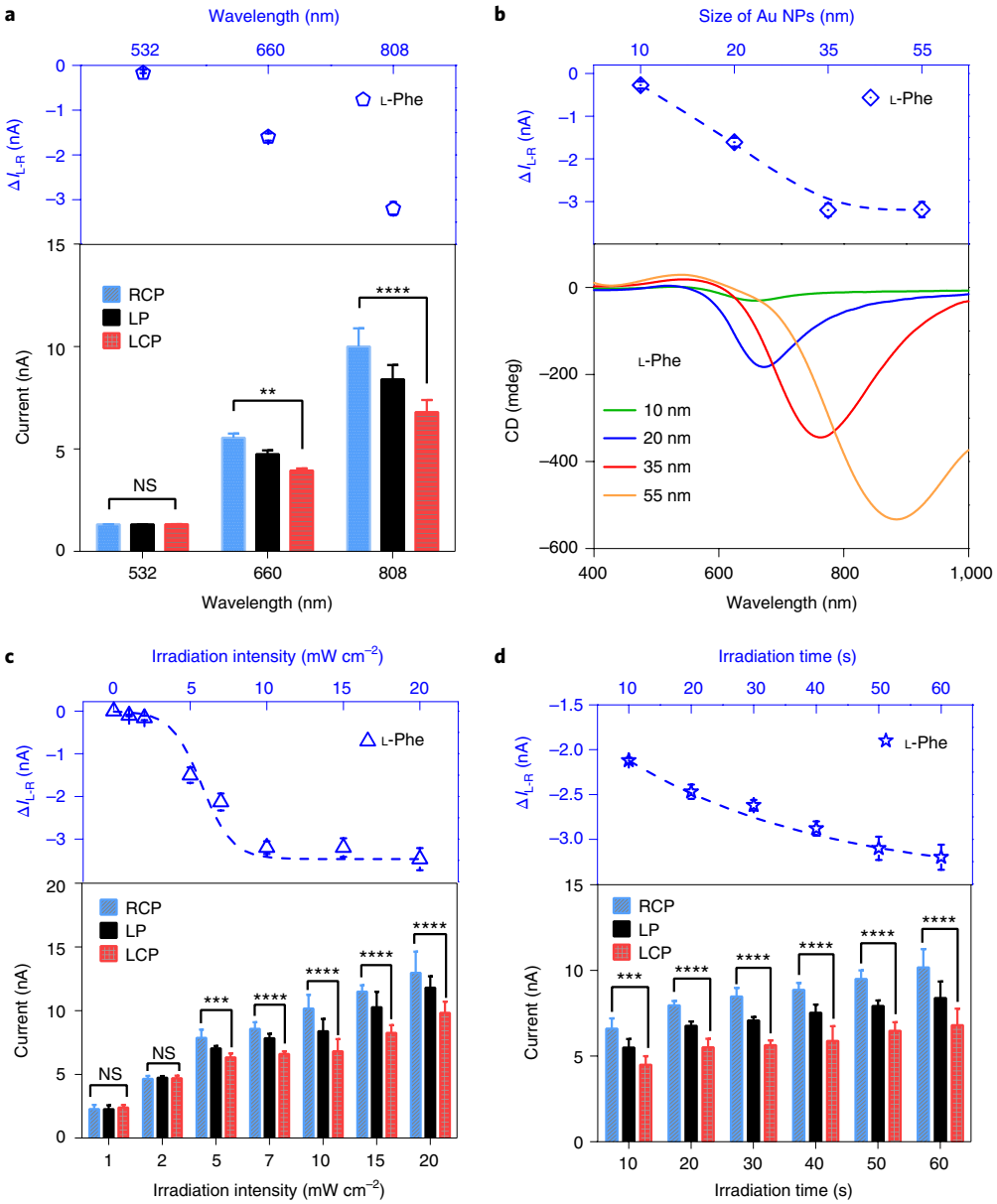

Fig. 2 | Photocurrent generation across nanofilms from L-Phe-NPs. a, ΔI_{L-R} (top) and I (bottom) observed for CPL illumination with different wavelengths. An 808 nm light source showed a high photocurrent of 6.82–10.04 nA and $\Delta I_{L-R} = 3.22$ nA. In contrast, CPL irradiation at 532 nm generated a photocurrent of 1.32 nA; there was no significant difference between LCP and RCP within the error range. CPL with a wavelength of 660 nm generated a photocurrent of 3.95–5.55 nA, and the difference between LCP and RCP was 1.60 nA, which was not as large as that observed at 808 nm. **b**, ΔI_{L-R} (top) and CD spectra (bottom) observed for nanofilms made from NPs of different sizes. Within this range of NP diameters, the larger the diameter, the higher the CD peak; the maximum-of-absorption peak tended to red shift as the diameter increased. ΔI_{L-R} present concomitant rise and eventual saturation for 35 nm NPs. **c**,**d**, ΔI_{L-R} (top) and I (bottom) observed for different illumination intensity (**c**) and exposure time (**d**). The I and ΔI_{L-R} values increased gradually as the illumination intensity and duration increased. The error bars represent the standard deviations of three independent tests.

heating. However, there were no statistically significant differences in the photothermal effects for nanofilms made from Cit-, DL-Phe-, L-Phe- or D-Phe-NPs, for which the photocurrent values exhibited large differences, suggesting that the photothermal effect was not responsible for ΔI_{L-R} (Supplementary Fig. 14).

Then, we tested whether I could be attributed to the irreversible photocatalytic oxidation of the Phe film on the NPs. However, Phe surface ligands remained unchanged under the illumination conditions used in our electrochemical experiments over numerous cycles (Supplementary Figs. 4 and 11). These data indicated that the photoinduced decomposition was not responsible for the observed photochemical effects.

We also considered the possible contribution of chiral-induced spin selectivity (CISS) effects[46], but the lack of response to the external magnetic field in different formats (Supplementary Fig. 15) as well as other tests, including the variation of different amino acids with specific orientation to the gold surface (Fig. 3c and Supplementary Fig. 10), indicated that the contribution of the CISS effects was too small to generate ΔI_{L-R} with a magnitude commensurate with the data shown in Fig. 2.

When the pore diameter becomes comparable to the Debye screening length, light–matter interactions in plasmonic films can also affect the ionic atmosphere and ion transport through the films[16–20]. Besides inorganic materials[47], coupled optical and ionic

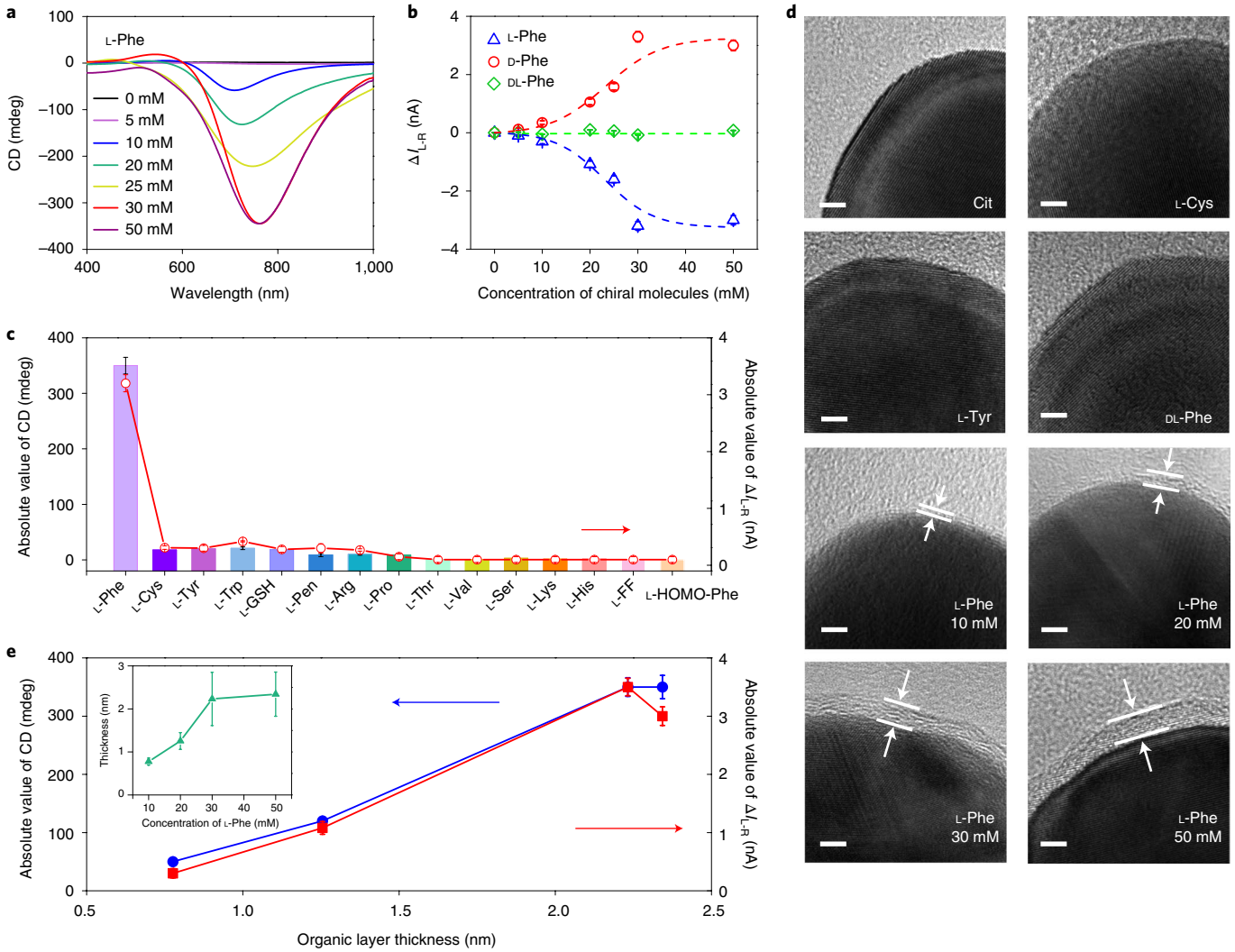

Fig. 3 | Uniqueness of Phe-NPs for generating CPL-dependent photocurrent. a, CD spectra of gold nanofilms modified at different concentrations of L-Phe. **b**, Dependence of ΔI_{L-R} on the concentration of Phe during the preparation of the gold nanofilms. **c**, CD amplitudes and ΔI_{L-R} values for NPs with different chiral surface ligands. Cys, cysteine; Tyr, tyrosine; Trp, tryptophan; GSH, glutathione; Pen, penicillamine; Arg, arginine; Pro, proline; Thr, threonine; Val, valine; Ser, serine; Lys, lysine; His, histidine; FF, diphenylalanine; HOMO-Phe, homophenylalanine. **d**, HRTEM images of Cit-stabilized gold nanofilms and gold nanofilms modified with L-Cys, L-Tyr or DL-Phe, and HRTEM images of the nanofilms after the addition of L-Phe at different concentrations during the surface modification of the NP membrane. The scale bars are 2 nm. **e**, CD amplitudes (blue) and ΔI_{L-R} changes (red) as a function of the thickness of the organic layer on the surfaces of NPs modified at different concentrations of L-Phe. Inset: the thickness of the organic layer on the surface of NPs modified at different concentrations of L-Phe. As the concentration of L-Phe in the solution used for surface modification increased, the thickness of the L-Phe layer on the surfaces of NPs gradually increased, reaching saturation at 30 mM Phe. The CD amplitudes and ΔI_{L-R} values showed the same changing trends as the thickness of the organic layer. The averages of three independent tests are plotted.

processes, also known as optoionic effects, may also occur in nanofilms from chiral NPs. When the electrolyte (KCl) concentration around the membrane approached 0.01 mM, no discernible photoeffect was observed. As the electrolyte concentration increased, ΔI_{L-R} increased and reached saturation at 10 mM. At any electrolyte concentration, the rise and decay times of $I(t)$ exceeded 10 s, which is characteristic of the diffusion of ions rather than electrons, and is consistent with expectations for ion fluxes induced by optical phenomena (Supplementary Fig. 16).

Based on the results described above, the polarization-sensitive photocurrent is attributed to the ejection of electrons[48,49] at the particle–medium interface[50,51]. These electrons are sometimes referred to as 'hot' electrons and they are analogous with photogenerated solvated electrons in the electromagnetic field of laser pulses[52]. Their chemical interactions with the delocalized orbitals of aromatic molecules in the medium can lead to entrapment enhanced by the coupling of chiral Phe and metallic NP cores, which subsequently induced ion transport to and from the NP interfaces. Although the ejected electrons are short-lived, continuous illumination causes a steady-state photocurrent at the NP–electrolyte interface, especially under conditions of the wave-guided resonance present in the nanofilms. The strong coupling between out-of-plane NP dipolar moments suppresses radiative decay, trapping light in the plane of the nanofilm and strongly localizing optical fields on each NP[38,39]. To probe this mechanism, the charge density at the NP–electrolyte interface arising from the ejection and entrapment of electrons was evaluated using density functional theory (DFT). Although NP models amenable to DFT simulations (Fig. 4a and Supplementary Fig. 17) are smaller than the particles used in the experiment, and do not have the same thick layer of organic ligands observed in

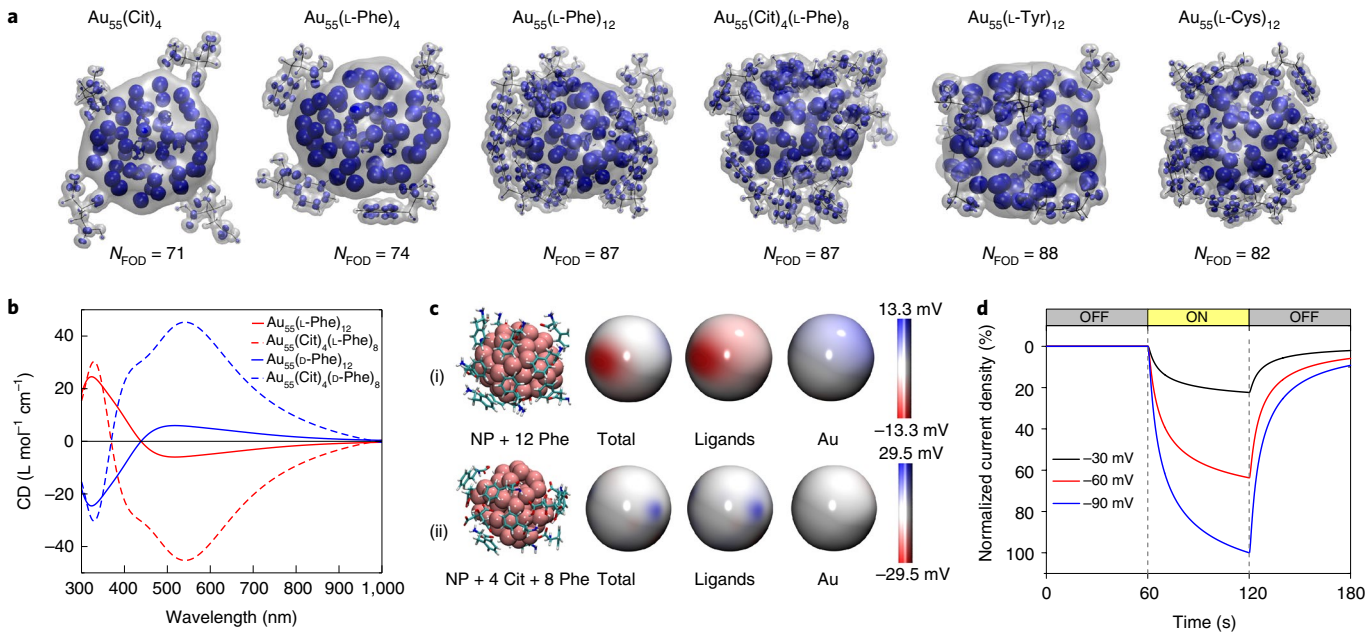

Fig. 4 | Photocurrent generation via plasmon-driven ejection of electrons to the particle–medium interface. a, FOD for different NP–ligand models. All FOD isosurfaces were obtained using 0.002 e/Bohr^3 and 0.02 e/Bohr^3 isovalues for semitransparent grey isosurfaces and opaque blue isosurfaces, respectively. Grey denotes the regions that can be accessible to ejected electrons; blue denotes the regions where they are more likely to be localized. **b**, CD spectra calculated for NPs decorated with either Phe or a mixture of Cit and Phe. **c**, DFT simulation of the average transient electrostatic potential distribution of Au_{55}(L-Phe)$_{12}$ and Au_{55}(Cit)$_4$(L-Phe)$_8$ under excitation by 808 nm photons. These results directly confirm that both systems produce a non-uniform electrostatic potential of tens of millivolts in the nearby solution, and the adsorbed ions are expected to move in response to the corresponding electric field. Au_{55}(Cit)$_4$(L-Phe)$_8$ shows a higher photoexcitation potential under light because it has a stronger solvated-electron-holding capacity. The spherical surfaces around the NPs correspond to the regions in which ions are expected to be adsorbed onto their surfaces. The total electrostatic potential was split into the contribution from the NPs and the ligands. **d**, The normalized photocurrent difference generated by the different transmembrane potentials driving the directional ion transport calculated with finite element simulations; the photocurrent kinetics were nearly identical to those observed experimentally.

the HRTEM images, the key features in their absorption and CD spectra were similar to those measured experimentally (Fig. 4b and Supplementary Fig. 2).

To further confirm the optoionic mechanism, we note that it necessitates the nanofilm to acquire negative charge at the NP–medium interface on illumination with visible light (Fig. 4c and Supplementary Videos 1 and 2). The dependence of electron excitation on the chemical structure of ligands can be evaluated by fractional occupation number weighted electron density (FOD), which enables calculating the average number of electrons at the NP–electrolyte interface (N_{FOD}). Comparison of NPs carrying Cit, L-Cys, L-Tyr and different numbers of Phe ligands shows that greater density of surface ligands and higher molecular mass increases N_{FOD}. For example, as the number of Phe ligands rose from 4 to 12, N_{FOD} increased from 74 to 87 (Fig. 4a), which is consistent with the observed rise in ΔI_{L-R} with increasing Phe surface density (Fig. 3a,b). These calculations also indicate that not only the surface density, but also the aromaticity of surface ligands play a role in accommodating temporarily entrapped electrons at the interface. As such, N_{FOD} values for Tyr and Phe are higher than for Cys. The total thickness of surface ligands is also essential for stabilizing photogenerated charges on NP surfaces, which directly affect I. The self-assembled 2.3 nm layer of Phe is approximately ten times thicker than the layers formed by other ligands. The thick layer of Phe entraps electrons in the interfacial region more efficiently than the much thinner layer of Tyr. Such entrapment increases the steady-state concentration of charges at the interface, with the electronic processes being similar to the electron entrapment at semiconductor–gold interfaces[49].

The increase of the negative charge at the NP–water interface on illumination, manifesting as polarization-dependent photovoltage (Fig. 1j,k) causes migration of ions through the network of nanoscale channels formed by NPs. The kinetics of the resulting photocurrent calculated by finite element simulations show temporal dependence identical to those observed in the experiment (Fig. 4d and Supplementary Fig. 18). Photocurrent at different wavelengths and in the nanofilms made from differently sized NPs (based on the Poisson–Nernst–Planck equation) also agree very well with experimental results (Supplementary Tables 2 and 3).

Detection of circular polarization with multilayer nanofilms. The optimal conditions for CPL detection using chiral NP membranes were examined to better understand the advantages and disadvantages of polarization-sensitive optoionic effects compared to other technical solutions in chiral photonics. The multilayer films were fabricated by consecutively transferring NP monolayers onto an AAO support (Supplementary Fig. 19). As the number of NP layers increased, the CD amplitude increased significantly from monolayers to bilayers to trilayers, reaching 950 mdeg for the 3L nanofilms (Fig. 5a). The photocurrent also increased, with ΔI_{L-R} reaching 6.43 nA for 3L nanofilms (Fig. 5b). This value represents a large electronic read-out for RCP light, 1.87-fold higher than under LCP illumination and exceeding the photovoltage/photocurrent differences for circularly polarized states on incident photons of organic, inorganic and metastructured thin films[40,41]. Moreover, the ratio between photocurrent obtained for RCP and LCP was as high as 2.20-fold and 2.41-fold for 5L and 10L nanofilms, respectively (Fig. 5c,d). Importantly, $I(t)$ profiles for the nanofilms from

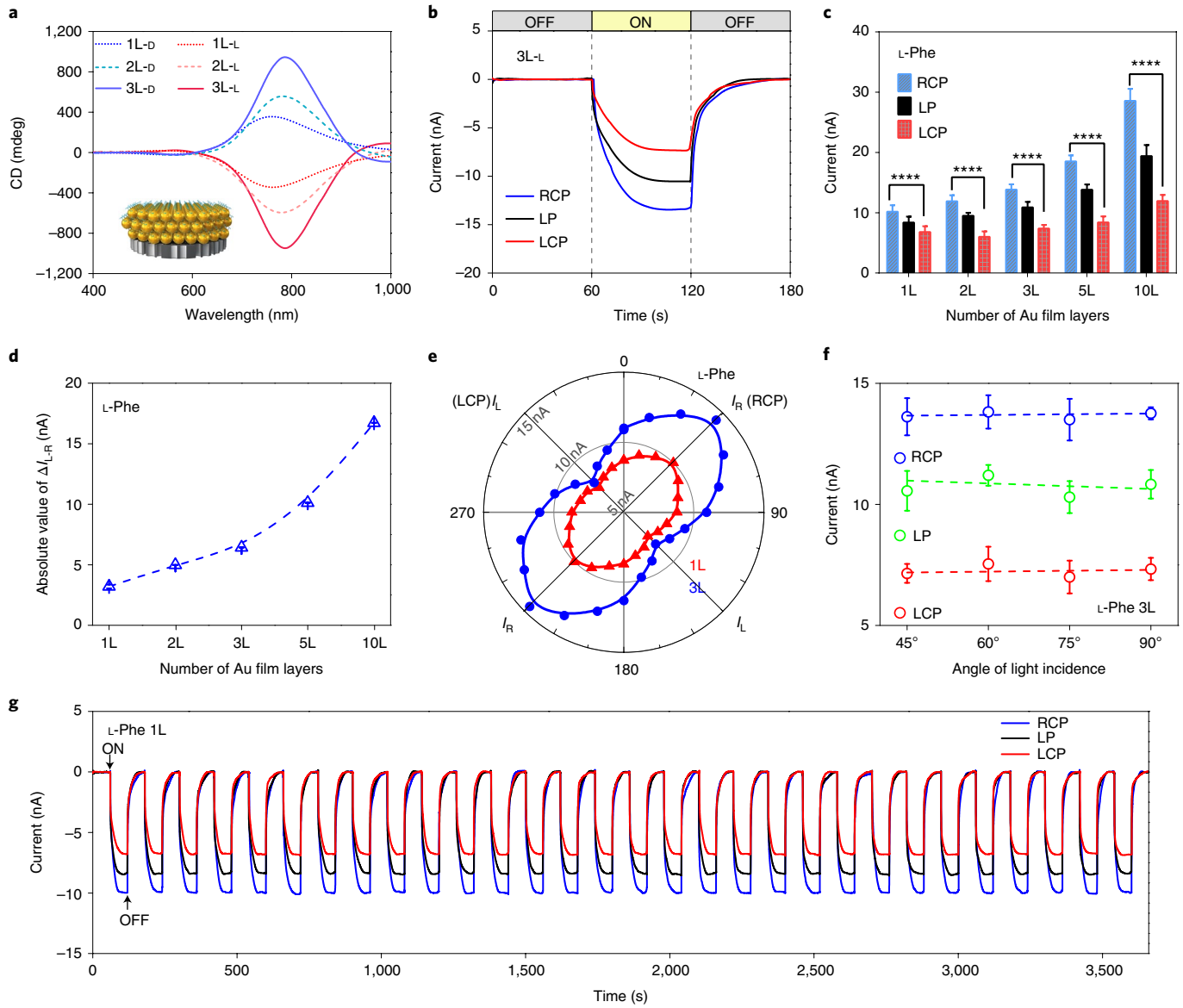

Fig. 5 | CPL detection using multilayer nanofilms. a, CD spectra of monolayer (1L), bilayer (2L) and three-layer (3L) NP films. **b**, *I* registered for 3L nanofilms from L-Phe-modified NPs under CPL illumination. **c**,**d**, Dependence of *I* (**c**) and ΔI_{L-R} (**d**) on the number of layers in L-Phe-modified nanofilms; 5L, five layers; 10L, ten layers. **e**, Polar plots of the polarization dependence of the photocurrent of 1L and 3L nanofilms from L-Phe-modified NPs. The length of the vector from the centre of the coordinates to the point on the curve is equal to *I*. The polar angle represents the angle of rotation of the quarter-wave plate and the degree of incident light ellipticity. **f**, The photocurrent measurements for the 3L nanofilms from L-Phe-modified NPs irradiated with light at different incident angles (that is, the angle between the light and the surface of the nanofilm). The error bars represent the standard deviations of three independent tests. **g**, Stability tests of photocurrent under CPL illumination. Photocurrent generated by the CPL-illuminated nanofilm was reproducible over 30 on–off cycles. Similar results were obtained for $n = 3$ independent nanofilm samples.

L-Phe- or D-Phe-NPs did not show any evidence of degradation for multiple on–off cycles under LCP and RCP illumination (Fig. 5g and Supplementary Fig. 20).

Finally, by rotating the quarter-wave plate at different angles under illumination, we found that the degree of polarization of light affected the intensity of the photocurrent. The established relationship between *I* and the degree of light polarization enables accurate detection of the ellipticity of the incident light beam (Fig. 5e and Supplementary Fig. 21). Importantly, the detection of CPL was equally accurate regardless of the incident angle, which vividly differentiates our NP-based films from metasurfaces and other polarization-sensitive optoelectronic prototypes (Fig. 5f and Supplementary Fig. 22).

Conclusions

The unexpectedly strong sensitivity of photocurrent to polarization was observed for chiroptically active nanofilms from gold NPs with a uniquely thick self-assembled layer of phenylalanine. The differentiation between RCP and LCP exceeds that previously observed for thin chiral films of organic or inorganic materials by 1–2 orders of magnitude, which is attributed to wave-guided chiroplasmonic modes propagating along the nanofilm surface and charge entrapment in chiral surface ligands around the NPs. Although metamaterials with optoelectronic effects exhibit shorter response times[6,7], manufacturing with self-assembled NP films offers the benefit of simplicity, scalability and energy efficiency. The high CPL contrast of the photocurrent opens the path to the application of

plasmonic materials-based chiral photonics. These findings present the possibility of mimicking the polarization vision of animals in non-biological nanoscale constructs. Integration with microfluidic devices and the absence of incident angle dependence offer the opportunity for conformal technological replicas of CPL-sensitive organs for utilization in machine vision. Further explorations are expected towards constructing optoionic membranes with enhanced mirror asymmetry to improve the polarization recognition characteristics. Furthermore, incorporation of chiral NPs with high *g*-factors[53] and chiral perovskites[54] can lead to their implementation in optical computing and telecommunication technologies.

Online content

Any methods, additional references, Nature Research reporting summaries, source data, extended data, supplementary information, acknowledgements, peer review information; details of author contributions and competing interests; and statements of data and code availability are available at https://doi.org/10.1038/s41565-022-01079-3.

Received: 22 March 2021; Accepted: 13 January 2022;
Published online: 14 March 2022

References

1. McIver, J. W., Hsieh, D., Steinberg, H., Jarillo-Herrero, P. & Gedik, N. Control over topological insulator photocurrents with light polarization. *Nat. Nanotechnol.* **7**, 96–100 (2011).
2. Hatano, T., Ishihara, T., Tikhodeev, S. G. & Gippius, N. A. Transverse photovoltage induced by circularly polarized light. *Phys. Rev. Lett.* **103**, 103906 (2009).
3. Bai, Q. Manipulating photoinduced voltage in metasurface with circularly polarized light. *Opt. Express* **23**, 5348–5356 (2015).
4. Yokoyama, A., Yoshida, M., Ishii, A. & Kato, Y. K. Giant circular dichroism in individual carbon nanotubes induced by extrinsic chirality. *Phys. Rev. X* **4**, 011005 (2014).
5. Ma, Q. et al. Direct optical detection of Weyl fermion chirality in a topological semimetal. *Nat. Phys.* **13**, 842–847 (2017).
6. Yang, Y., da Costa, R. C., Fuchter, M. J. & Campbell, A. J. Circularly polarized light detection by a chiral organic semiconductor transistor. *Nat. Photon.* **7**, 634–638 (2013).
7. Li, W. et al. Circularly polarized light detection with hot electrons in chiral plasmonic metamaterials. *Nat. Commun.* **6**, 8379 (2015).
8. Wang, Y. H., Steinberg, H., Jarillo-Herrero, P. & Gedik, N. Observation of Floquet–Bloch states on the surface of a topological insulator. *Science* **342**, 453–457 (2013).
9. Higuchi, T., Heide, C., Ullmann, K., Weber, H. B. & Hommelhoff, P. Light-field-driven currents in graphene. *Nature* **550**, 224–228 (2017).
10. Aca, E. T., Buchsbaum, S. F., Combs, C., Fornasiero, F. & Siwy, Z. S. Biomimetic potassium-selective nanopores. *Sci. Adv.* **5**, eaav2568 (2019).
11. Cheng, C., Jiang, G., Simon, G. P., Liu, J. Z. & Li, D. Low-voltage electrostatic modulation of ion diffusion through layered graphene-based nanoporous membranes. *Nat. Nanotechnol.* **13**, 685–690 (2018).
12. Wang, R. et al. Temperature-sensitive artificial channels through pillar[5] arene-based host-guest interactions. *Angew. Chem. Int. Ed. Engl.* **56**, 5294–5298 (2017).
13. Zhang, Z. et al. Improved osmotic energy conversion in heterogeneous membrane boosted by three-dimensional hydrogel interface. *Nat. Commun.* **11**, 875 (2020).
14. Schroeder, T. B. H. et al. An electric-eel-inspired soft power source from stacked hydrogels. *Nature* **552**, 214–218 (2017).
15. Sun, Y. et al. A biomimetic chiral-driven ionic gate constructed by pillar[6] arene-based host-guest systems. *Nat. Commun.* **9**, 2617 (2018).
16. Sun, Y. et al. A light-regulated host-guest-based nanochannel system inspired by channelrhodopsins protein. *Nat. Commun.* **8**, 260 (2017).
17. Xie, X., Crespo, G. A., Mistlberger, G. & Bakker, E. Photocurrent generation based on a light-driven proton pump in an artificial liquid membrane. *Nat. Chem.* **6**, 202–207 (2014).
18. Mourot, A. et al. Rapid optical control of nociception with an ion-channel photoswitch. *Nat. Methods* **9**, 396–402 (2012).
19. White, W., Sanborn, C. D., Reiter, R. S., Fabian, D. M. & Ardo, S. Observation of photovoltaic action from photoacid-modified Nafion due to light-driven ion transport. *J. Am. Chem. Soc.* **139**, 11726–11733 (2017).
20. Xiao, K. et al. Artificial light-driven ion pump for photoelectric energy conversion. *Nat. Commun.* **10**, 74 (2019).
21. Palmer, B. A. et al. A highly reflective biogenic photonic material from core-shell birefringent nanoparticles. *Nat. Nanotechnol.* **15**, 138–144 (2020).
22. Roberts, N. W., Chiou, T. H., Marshall, N. J. & Cronin, T. W. A biological quarter-wave retarder with excellent achromaticity in the visible wavelength region. *Nat. Photon.* **3**, 641–644 (2009).
23. Chiou, T. H. et al. Circular polarization vision in a stomatopod crustacean. *Curr. Biol.* **18**, 429–434 (2008).
24. Tang, Z. et al. Photo-driven active ion transport through a Janus microporous membrane. *Angew. Chem. Int. Ed. Engl.* **59**, 6244–6248 (2020).
25. Yang, J. et al. Photo-induced ultrafast active ion transport through graphene oxide membranes. *Nat. Commun.* **10**, 1171 (2019).
26. Xiao, K. et al. Photo-driven ion transport for a photodetector based on an asymmetric carbon nitride nanotube membrane. *Angew. Chem. Int. Ed. Engl.* **58**, 12574–12579 (2019).
27. Edel, J. B., Kornyshev, A. A., Kucernak, A. R. & Urbakh, M. Fundamentals and applications of self-assembled plasmonic nanoparticles at interfaces. *Chem. Soc. Rev.* **45**, 1581–1596 (2016).
28. Kotov, N. A., Meldrum, F. C., Wu, C. & Fendler, J. H. Monoparticulate layer and Langmuir–Blodgett-type multiparticulate layers of size-quantized cadmium sulfide clusters: a colloid-chemical approach to superlattice construction. *J. Phys. Chem.* **98**, 2735–2738 (1994).
29. Udayabhaskararao, T. et al. Tunable porous nanoallotropes prepared by post-assembly etching of binary nanoparticle superlattices. *Science* **358**, 514–518 (2017).
30. Knoppe, S. & Bürgi, T. Chirality in thiolate-protected gold clusters. *Acc. Chem. Res.* **47**, 1318–1326 (2014).
31. Zhang, Q. et al. Unraveling the origin of chirality from plasmonic nanoparticle–protein complexes. *Science* **365**, 1475–1478 (2019).
32. Chen, W. et al. Nanoparticle superstructures made by polymerase chain reaction: collective interactions of nanoparticles and a new principle for chiral materials. *Nano Lett.* **9**, 2153–2159 (2009).
33. Ma, W. et al. Chiral inorganic nanostructures. *Chem. Rev.* **117**, 8041–8093 (2017).
34. Ben-Moshe, A., Maoz, B. M., Govorov, A. O. & Markovich, G. Chirality and chiroptical effects in inorganic nanocrystal systems with plasmon and exciton resonances. *Chem. Soc. Rev.* **42**, 7028–7041 (2013).
35. Ebbesen, T. W., Lezec, H. J., Ghaemi, H. F., Thio, T. & Wolff, P. A. Extraordinary optical transmission through sub-wavelength hole arrays. *Nature* **391**, 667–669 (1998).
36. Zhao, J., Li, B., Onda, K., Feng, M. & Petek, H. Solvated electrons on metal oxide surfaces. *Chem. Rev.* **106**, 4402–4427 (2006).
37. Matricardi, C. et al. Gold nanoparticle plasmonic superlattices as surface-enhanced Raman spectroscopy substrates. *ACS Nano* **12**, 8531–8539 (2018).
38. Wang, D., Guan, J., Hu, J., Bourgeois, M. R. & Odom, T. W. Manipulating light–matter interactions in plasmonic nanoparticle lattices. *Acc. Chem. Res.* **52**, 2997–3007 (2019).
39. Mueller, N. S. et al. Deep strong light–matter coupling in plasmonic nanoparticle crystals. *Nature* **583**, 780–784 (2020).
40. Lee, S. H. et al. Highly photoresponsive and wavelength-selective circularly-polarized-light detector based on metal-oxides hetero-chiral thin film. *Sci. Rep.* **6**, 19580 (2016).
41. Chen, C. et al. Circularly polarized light detection using chiral hybrid perovskite. *Nat. Commun.* **10**, 1927 (2019).
42. Do, T. D., Kincannon, W. M. & Bowers, M. T. Phenylalanine oligomers and fibrils: the mechanism of assembly and the importance of tetramers and counterions. *J. Am. Chem. Soc.* **137**, 10080–10083 (2015).
43. Singh, V., Rai, R. K., Arora, A., Sinha, N. & Thakur, A. K. Therapeutic implication of L-phenylalanine aggregation mechanism and its modulation by D-phenylalanine in phenylketonuria. *Sci. Rep.* **4**, 3875 (2014).
44. Amdursky, N. & Stevens, M. M. Circular dichroism of amino acids: following the structural formation of phenylalanine. *ChemPhysChem* **16**, 2768–2774 (2015).
45. Xia, Y. et al. Self-assembly of self-limiting monodisperse supraparticles from polydisperse nanoparticles. *Nat. Nanotechnol.* **6**, 580–587 (2011).
46. Naaman, R., Paltiel, Y. & Waldeck, D. H. Chiral molecules and the electron spin. *Nat. Rev. Chem.* **3**, 250–260 (2019).
47. Senocrate, A., Kotomin, E. & Maier, J. On the way to optoionics. *Helv. Chim. Acta* **103**, e2000073 (2020).
48. Brongersma, M. L., Halas, N. J. & Nordlander, P. Plasmon-induced hot carrier science and technology. *Nat. Nanotechnol.* **10**, 25–34 (2015).
49. Clavero, C. Plasmon-induced hot-electron generation at nanoparticle/metal-oxide interfaces for photovoltaic and photocatalytic devices. *Nat. Photon.* **8**, 95–103 (2014).
50. Nakanishi, H. et al. Photoconductance and inverse photoconductance in films of functionalized metal nanoparticles. *Nature* **460**, 371–375 (2009).
51. Cortes, E. et al. Plasmonic hot electron transport drives nano-localized chemistry. *Nat. Commun.* **8**, 14880 (2017).

52. Hapiot, P., Konovalov, V. V. & Saveant, J.-M. Application of laser pulse photoinjection of electrons from metal electrodes to the determination of reduction potentials of organic radicals in aprotic solvents. *J. Am. Chem. Soc.* **117**, 1428–1434 (1995).
53. González-Rubio, G. et al. Micelle-directed chiral seeded growth on anisotropic gold nanocrystals. *Science* **368**, 1472–1477 (2020).
54. Di Nuzzo, D. et al. Circularly polarized photoluminescence from chiral perovskite thin films at room temperature. *ACS Nano* **14**, 7610–7616 (2020).

Methods

Preparation of chiral Au NPs. An Au NP colloid dispersion ($d = 35.1 \pm 0.8$ nm) was synthesized by the citrate reduction of chloroauric acid ($HAuCl_4$) in the aqueous phase[55]. In brief, 6 ml of 10 mM $HAuCl_4$ solution was added to 195 ml of deionized water and boiled. Then, 3.2 ml of 10% w/v sodium citrate solution and 1.5 ml of 5 nm Au seed solution were added, and the mixture was boiled for 20 min to generate a stable colloid solution of Au NPs. The NPs were concentrated tenfold by centrifugation and resuspended in a 10 mM carbonate buffer solution to obtain a high-concentration Au NP solution. Finally, the desired amount of Phe was added, and the solution was incubated for 2 h at 60 °C. The average particle diameters were determined using TEM on a JEOL JEM-2100 transmission electron microscope (operated at an acceleration voltage of 200 kV). Differently sized Au NPs were synthesized by adjusting the amount of sodium citrate added. The sizes of the NPs were confirmed with a Zetasizer Nano ZS (Malvern) equipped with a 632.8 nm laser.

Preparation of chiroplasmonic membranes. Free-standing nanofilms were formed at a water–oil interface using an aqueous solution of the chiral Au NPs and an *n*-hexane phase. The self-assembly of the NPs at the interface was induced by the slow addition of ethanol[27,56]. The *n*-hexane phase was then allowed to evaporate slowly, and the nanofilm was transferred to an AAO membrane using monolayer lift-off onto a solid support. The AAO membrane with a pore diameter of 20 nm, a thickness of 60 μm and a pore density of 10^{11} per cm^2 (Puyuan Hefei Nano) was used as a self-supporting porous template.

Electrochemical measurements. The NP–AAO membranes were placed between two Plexiglass cells with holes 3 mm in diameter. A KCl solution (2 ml) was added to each of the two chambers. A pair of Ag/AgCl electrodes and a CHI-760 electrochemical workstation (CHI) were used to record the change in current over time[57]. CPL with different polarization directions was produced by adjusting a quarter-wave plate. During the test, the change in the current was monitored as the light was turned on and off. Unless otherwise specified, the wavelength used for irradiation was 808 nm, the light intensity was 10 mW cm^{-2} and the duration of irradiation ('on') and the interval ('off') between two irradiation cycles were 60 s.

Statistics and reproducibility. Experimental errors were calculated as the standard error of the mean, with *n* referring to the number of analysed samples and reported in the figure legends.

Data availability

Source data are provided with this paper. All data that support the findings of this study have been included in the main text and Supplementary Information. Any additional materials and data are available from the corresponding authors on reasonable request.

References

55. Zhao, X. et al. Tuning the interactions between chiral plasmonic films and living cells. *Nat. Commun.* **8**, 2007 (2017).
56. Hu, L., Chen, M., Fang, X. & Wu, L. Oil–water interfacial self-assembly: a novel strategy for nanofilm and nanodevice fabrication. *Chem. Soc. Rev.* **41**, 1350–1362 (2012).
57. Gao, J., Feng, Y., Guo, W. & Jiang, L. Nanofluidics in two-dimensional layered materials: inspirations from nature. *Chem. Soc. Rev.* **46**, 5400–5424 (2017).

Acknowledgements

C.X. acknowledges support from the National Key Research and Development Program of China (grant no. 2017YFA0206902), W.Z. acknowledges support from the National Key Research and Development Program of China (grant no. 2017YFA0303400), H.K., L.X. and M.S. acknowledge support from the National Natural Science Foundation of China (grant nos. 21925402, 32071400 and 21977038), H.K. acknowledges support from the Natural Science Foundation of Jiangsu Province (grant no. BK20212014), W.Z. acknowledges support from the National Natural Science Foundation of China (grant nos. 11774036 and 12174032) and from the National Natural Science Foundation of China/Research Grants Council (grant no. 11861161002). N.A.K. is grateful for support from the National Science Foundation via projects NSF 1463474 "Energy- and Cost-Efficient Manufacturing Employing Nanoparticles" and NSF 1566460 "Nanospiked Particles for Photocatalysis". R.K. acknowledges support from the Minerva Foundation with funding from the Federal German Ministry for Education and Research. F.M.C., W.R.G., M.C.S., E.B.C.-N., E.C.P. and A.F.M. are grateful to the Brazilian funding agencies CAPES (finance code 001), CNPq-INCT (573742/2008-1) and FAPESP (2012/15147-4, 2013/07296-2, 2014/50249-8, 2015/12851-0 and 2017/11986-5) for financial support and the HPC resources provided by the SDumont supercomputer at the National Laboratory for Scientific Computing (LNCC/MCTI, Brazil; http://sdumont.lncc.br) and by the Cloud@UFSCar (https://www.sin.ufscar.br). A.F.M. is grateful to MEC/PET for a fellowship and to CNPq for a research fellowship.

Author contributions

H.K., R.K., N.A.K. and C.X. conceived the project and designed the experiments. J.C. was responsible for electrochemical, CD and CPL measurements. W.Z. was responsible for the calculations of optical response (absorption and circular dichroism) and photocurrent calculations based on the Poisson–Nernst–Planck equation. L.X. and C.H. performed the HRTEM, TEM, SEM and AFM experiments. L.X. and W.M. carried out the preparation of gold nanofilms. M.S. and X.W. were responsible for the synthesis and modification of gold NPs with different particle sizes. F.M.C., W.R.G., M.C.S., E.B.C.-N., E.C.P. and A.F.de.M. designed, executed and analysed the simulations of DFT calculations, electrodynamics calculations and finite element calculations and wrote the corresponding text. R.A.L.V., X.L., X.Q. and J.X. carried out calculations related to the interaction between Phe and gold. H.K. and N.A.K. conceptualized the work. C.X. supervised the study. H.K., R.K., N.A.K. and C.X. analysed and discussed the results and wrote the manuscript.

Competing interests

The authors declare no competing interests.

Additional information

Supplementary information The online version contains supplementary material available at https://doi.org/10.1038/s41565-022-01079-3.

Correspondence and requests for materials should be addressed to Chuanlai Xu, Rafal Klajn, Nicholas A. Kotov or Hua Kuang.

Peer review information *Nature Nanotechnology* thanks Malcolm Kadodwala, Stefan Meskers and the other, anonymous, reviewer(s) for their contribution to the peer review of this work.